Status report on the WP2 of the Swiss-Danish instrumentation work packages for the European Spallation Source, ESS

focusing reflectometer for small samples

Selene guide concept

Selene
focusing reflectometer

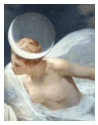

February 5, 2013

Swiss-Danish instrument initiative
WP 2
reflectometer

Jochen Stahn
Uwe Filges
Panagiotis Korelis
Emmanouela Rantsiou
Tobias Panzner

Ursula Hansen

Paul Scherrer Institut

UNIVERSITY OF COPENHAGEN

project team

Jochen Stahn	Laboratory for Neutron Scattering Paul Scherrer Institut Switzerland jochen.stahn@psi.ch +41 56 310 2518	senior scientist - project leader - concept - experiements
Panagiotis Korelis	Laboratory for Neutron Scattering Paul Scherrer Institut Switzerland panagiotis.korelis@psi.ch +41 56 310 5813	post-doc - McStas (gravity)
Uwe Filges	Laboratory for Developments and Methods Paul Scherrer Institut Switzerland uwe.filges@psi.ch +41 56 310 4606	senior scientist - McStas, MCNPX
Tobias Panzner	Laboratory for Developments and Methods Paul Scherrer Institut Switzerland tobias.panzner@psi.ch +41 56 310 4342	pst-doc - McStas - experiements
Emmanouela Rantsiou	Laboratory for Developments and Methods Paul Scherrer Institut Switzerland emmanouela.rantsiou@psi.ch +41 56 310 4631	pst-doc - McStas, MCNPX
Marité Cardenas	Nano-Science Center University of Copenhagen cardenas@nano.ku.dk +45 35 320 431	senior scientist - scientific advice
Ursula Bengaard Hansen	Nano-Science Center University of Copenhagen uhansen@fys.ku.dk +45 60 478 615 (mobile)	student assistant - McStas - experiements
Beate Klösgen	Department for Physics, Chemistry and Pharmacy University of Southern Denmark Denmark kloesgen@sdu.dk +45 6550 2561	associate professor - scientific advice

Selene moon, dark side titan goddess

detail of the ceiling painting
Selene and Endymion
at the
Ny Carlsberg Glyptotek, Copenhagen

contents

introduction

This document reports on the conceptual development of a focusing reflectometer, its prototyping and adaption to the European Spallation Source.

The *Swiss-Danish Instrument Initiative* proposes to build several, but highly optimised reflectometers, rather than one flexible instrument with moderate performance due to the necessary compromises. As "guiding ideas" we suggest I a small sample size, II a horizontal sample interface, and eventually III high resolution in q_y (i.e. GISANS).

Optimisation requirements of I and II exclude each other to some extend: The vertical scattering plane imposes quite severe constraints for high-angle diffraction, and gravitation effects become important. On the other side typical samples with liquid/liquid or liquid/gas interfaces are larger than $10 \times 10\,\mathrm{mm}^2$, while really *small* samples are below $1 \times 1\,\mathrm{mm}^2$. For measurements on horizontal surfaces it is often of advantage to sample a wide q_z range without changing the sample position, and without extensive reconfiguration of optical elements. On pulsed sources this results in a short instrument to allow for a wide λ range. Without this constraint it might be favourable to build a longer instrument to reduce background and to allow for more convenient beam manipulation.

We propose the usage of point-to-point focusing rather than a straight guide. This leads to a drastically reduced beam intensity in the guide, while almost conserving the phase space density actually needed for the measurements. Also the beam is convergent at the sample which avoids over-illumination of the sample (if required) and of the sample environment.

The idealised set-up consists of two subsequent identical guides (see sketch below and figure 1.1). Each guide has one reflecting surface shaped like one branch of an ellipse for each direction (like a Montel optics as used at synchrotron beam lines).

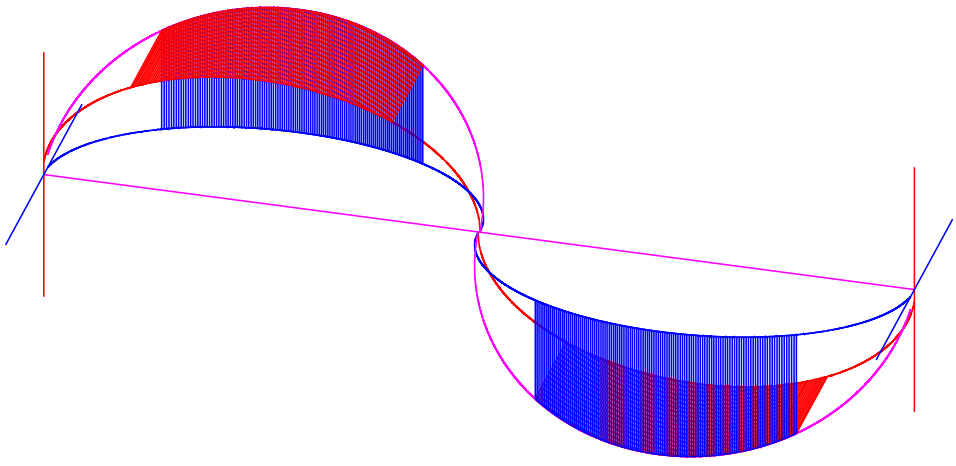

The (virtual) source is mapped by the first guide to an intermediate image, which is than mapped to the sample position. This way the coma aberration inherent to elliptic reflectors is almost completely corrected for. The maximum divergence $\Delta\theta$ is given by the acceptance of the first ellipse. It can be reduced by an aperture in between the focal planes. The spot-size at the sample position is (almost) identical to the source size, i.e. it can be adjusted by slits at the first focal point without changing $\Delta\theta$. With reference to the half-elliptic shape of the light-to-shadow border on the moon we call this the *Selene* set-up.

In the following chapter the generic lay-out of the instrument is presented, followed by a discussion of its components from source to detector. The design and realisation of a prototype *Selene* guide is presented in chapter 2. Based on these two possible realisations for the ESS are presented, one optimised for small samples (with horizontal scattering plane, chapter 3) and one optimised for liquid interfaces (chapter **??**).

history The idea for the *Selene* guide is based on concepts of F. Ott to use a focused beam with a wide divergence, and in combination a λ-θ encoding obtained by a graded monochromator of half-elliptic shape.[1, 2] First experiments with a graded multilayer coating [3] revealed conceptual problems and led to the approach to use a flat multilayer monochromator for λ-θ encoding, followed by the elliptic reflector. And attempts to correct for coma aberration finally led to the *Selene* guide geometry with two subsequent elliptic reflectors. This way, neutron guide and encoding are decoupled. I.e. encoding is optional and might be also achieved by other approaches like the *rainbow* concept by R. Cubitt.[4, 5]

Though developed for a reflectometer, the *Selene* guide concept can in principle used also for other instruments. The limiting factors are the transported divergence, the minimum wavelength, and the sample size.

Analytically this can be shown by using eqn. 1.3.4 and $\alpha_2\alpha_1' = \alpha_3\alpha_2' = (b/a)^2$, $\alpha_2 = \alpha_2'$. For the final image z_3 one gets

$$z_3(\alpha_3) \approx z_2(\alpha_2)\frac{(b/a)^2}{\alpha_3^2} \approx z_1\frac{(b/a)^2}{\alpha_2^2}\frac{(b/a)^2}{\alpha_3^2} \approx z_1 \tag{1.3.5}$$

This is illustrated in figure 1.7. The maps show $I(\theta, z)$ as accepted by the elliptic reflectometer (left), the corresponding intermediate image with the distorted shape (middle) and the almost restored shape at the image (source) position. The deviations still visible originate from the final length of the second reflectometer, and from the quite large pre-image chosen to emphasise the effect of coma aberration.

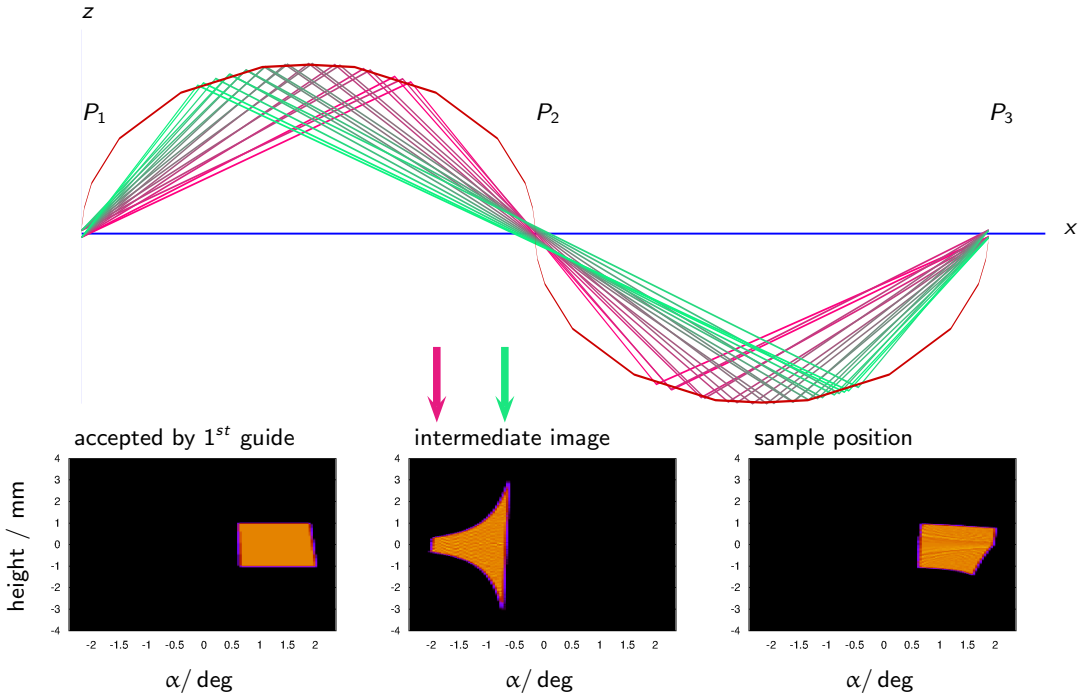

Figure 1.7: Sketch to illustrate the effect of coma aberration. The pre-image consists of 2 point-sources, located at $z = \pm 1$ mm. The half-axis parameters used here are $a = 2000$ mm, $b = 50$ mm, the sketch is stretched by 30 normal to the long axis. The take-off angle α is encoded in the colour of the beam. At the intermediate position a clear separation of the colours can be seen. High α result in an almost parallel wide beam, while low α result on a beam focused to the second focal point. Behind the second ellipse, the initial image is almost restored. The $I(\alpha, z)$ maps illustrate the shape of the phase space as accepted by the ellipse and defined by a 2 mm slit at P_1 (left), at the intermediate position P_2 (middle), and finally after correction at P_3 (right). The arrows atop the middle map denote for which α the beam is compressed (red) or expanded (green).

It is not always useful to correct for coma aberration: If e.g. a small beam is required, on can reach this by using the beam reflected at the end of the reflector. For the presented case its height is 30% of the initial slit, only. On the other side one can get a wide beam of low divergence by using the beginning of the reflector, only. This is what at synchrotron sources is achieved with a Kirkpatrick-Baez optics (which consists of two elliptically shaped reflectors, one for each direction).

1.3.3 chromatic aberration due to gravity

P. Korelis, E. Rantsiou

While the focusing properties of reflecting optics are achromatic (besides the λ dependent reflectivity) for straight trajectories, there are chromatic effects induced by gravity. Its influence on the spot size and divergence is not immediately apparent because there are amplifying and compensating aspects for reflections on an elliptic guide. E.g. if one assumes the first reflection pointing downwards, gravity leads to a longer free flight path before the neutron hits the reflector. But it will hit it at a smaller angle.

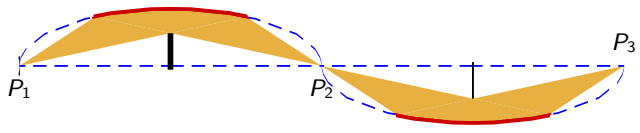

Figure 1.8: Sketch of the setup. The guide parameters are $c = 10\,000$ mm, $b/a = 0.0228$ and $\xi = 0.5$. The initial slit has a height of 1 mm and is centred at the focal point.

The main question to be answered then is whether or not gravity set limitations to the focusing performance of a *Selene* guide at the sample position. To elucidate the effect of gravity, virtual studies using the McStas simulation software package have been performed.

The model instrument is comprised of a single *Selene* guide with the first element reflecting downwards and the second reflecting upwards as shown in figure 1.8. The geometrical parameters are the same for the horizontal (xy plane) and vertical (xz plane) elliptic reflectors: $b/a = 0.0228$, $\xi = 0.5$, and length of the focusing section $4c = 40$ m. The resulting angular acceptance is $\Delta\theta = 1.5°$.

To single out the effect of gravity and to better illustrate that, certain simplifications have been added to the model. Regarding reflector performance, the reflectors are constructed from ideal supermirrors, disregarding changes in supermirror reflectivity as a function of momentum transfer and effects such as absorption. A virtual source is used, with a uniform wavelength distribution extending from 2 to 10 Å, and it is located at the entrance focal point of the *Selene* guide. The size of the source is 1×1 mm^2 and its divergence is adjusted to compensate for the crooked neutron trajectories that might result in some of the long-wavelength neutrons missing the far end of the reflector. As a result, the entirety of the reflecting surface of the first *Selene* element is illuminated by neutrons of all wavelengths.

Figure 1.9 shows the intensity maps at the intermediate focal point P_2, simulated with and without including gravity (bottom and top row, respectively). To single out with which trajectory certain features in the intensity maps are related, the first and second half of the first guide element were interchangeably switched to be vertically absorbing. The horizontal reflection element was fully reflecting in all cases.

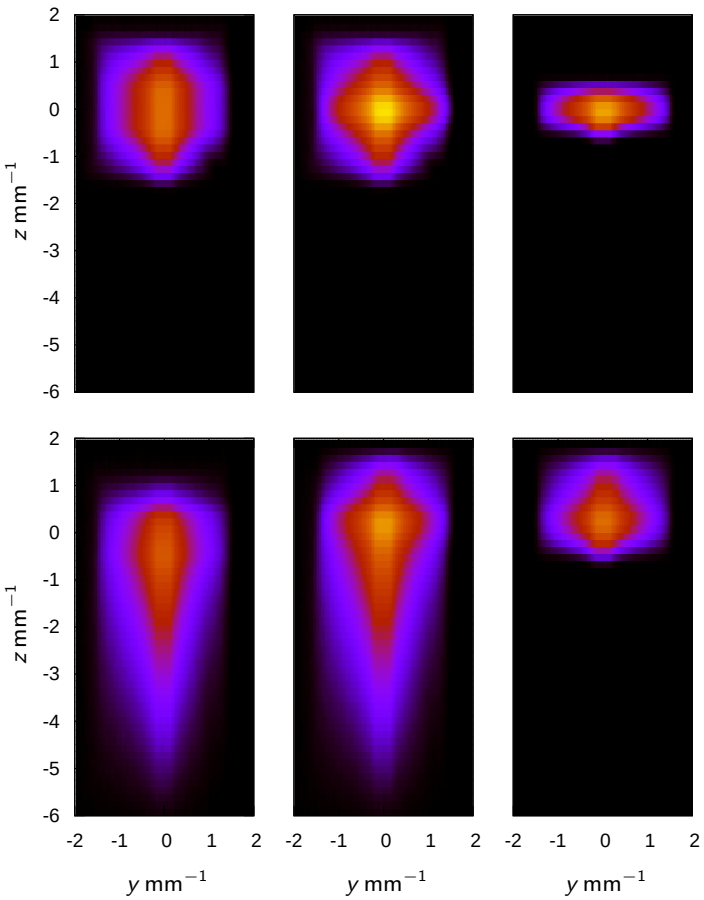

Figure 1.9: Intensity maps $\log_{10}[I(y,z)]$ at the intermediate focal point P_2 of a *Selene* guide system with a total length of 40 m. The upper row was simulated without gravity, the lower one with gravity. For the left/right column only the first/second half of the vertically reflecting guide element was actually reflecting. The middle column was obtained with reflection along the full guide element. The incident slit was 1×1 mm^2, the wavelength range was $\lambda \in [2, 10]$ Å.

The coma aberration, inherent to the elliptical shape of the reflectors, is evident in the intensity maps in the top row. Reflecting on the first half of the vertical elliptical reflector (left image) contributes a broad beam profile at P_2. In an inverse manner, reflecting on the second half of the vertical elliptical reflector (right image) results in a highly focused beam profile. As expected, the centre image in the top row, generated by reflecting on the complete first element, shows no difference in the intensity profile between the vertical and horizontal direction.

Gravity is included in the simulations shown in the bottom row. While no change in focusing is observed in the horizontal direction, a tail becomes visible in the vertical direction. Gravity does little to improve the focusing of neutrons reflected on the first half of the vertical elliptical reflector. The vertical tail is also shown to originate almost exclusively from reflections on the first half of the reflector. Reflections on the second half of the vertical elliptical reflector (bottom right image), are found to result in some smearing out of the bright focused spot, along the positive direction of the vertical axis. It was further clarified, through simulations using a single wavelength, that the vertical position of the focusing spot at P_2 shifts upwards, scaling with neutron wavelength. On one hand, the height of the focusing position for longer wavelengths is shifted upwards, and on the other hand, the long-wavelength neutrons are also more heavily influenced by gravity on their way to the second *Selene* element.

The intensity maps of the beam spot at the exit focal point P_3 are shown in figure 1.10, simulated with and without gravity. In the graph to the right, the intensity is integrated along the horizontal direction and the distribution of intensity as a function of the vertical position is shown for selected wavelengths.

Comparing the intensity maps, the beam profile appears to be close to fully restored. It becomes apparent that a compensating mechanism exists for the effect of gravity for small λ, once the neutrons have travelled through and interacted with the full length of the *Selene* guide. The integrated intensity as a function of vertical position indicates that for small wavelengths, e.g., 3 Å, the effect of gravity is negligible. For wavelengths near the upper end of the range that is expected at ESS for a *Selene* type reflectometer, there is an observable change, manifested by a vertical shift of the centre of the focused spot by approximately 0.3 mm, broadening at the base by nearly the same amount and a corresponding reduction in the intensity of the maximum plateau by about 15%.

The $I_\lambda(z)$ graph illustrates that there is only a week chromatic aberration up to at least 6 Å and a moderate effect at 9 Å. Above that the picture changes, the intensity for $\lambda = 15$ Å, for example, is distributed over 4.5 mm with a bimodal distribution. Obviously there is an upper limit for $x^2\,\lambda^2$, up to which the *Selene* guide has low chromatic aberration due to gravity.

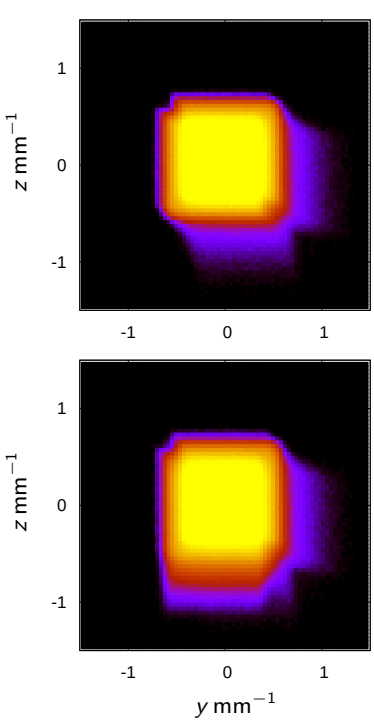

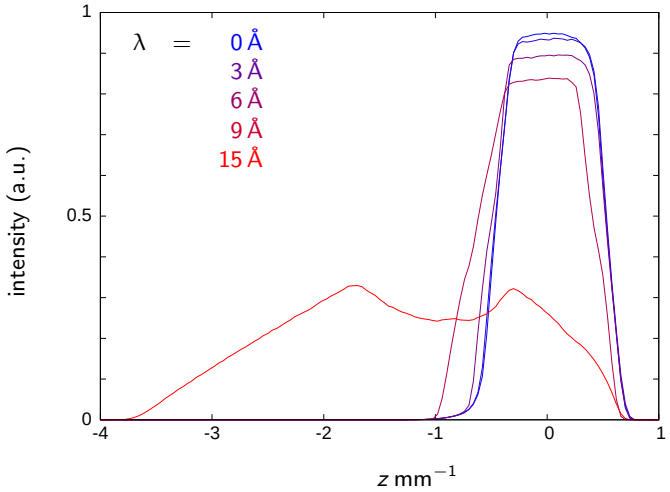

Figure 1.10: *Left:* Intensity maps $\log_{10}[\,I(y,z)\,]$ at the final focal point P_3 of a *Selene* guide system with a total length of 40 m. The upper map was simulated without gravity, the lower one with gravity. The incident slit was $1 \times 1\,\mathrm{mm}^2$, the wavelength range was $\lambda \in [2, 10]$ Å. *Top:* Intensity distributions $I(z) = \int I(y,z)\,\mathrm{d}y$ for wavelengths 0 Å (i.e. no gravity, green), 3 Å (red), and 9 Å (blue).

In a further set of simulations the geometry shown in figure 1.8 was turned upside down, i.e. the first guide element reflecting downwards and the second upwards. The essential difference is, that for longer wavelengths the intensity is reduced (some 10% at $\lambda = 9\,\text{Å}$), while the spot size is slightly smaller.

discussion Taking into account that the actual length of one *Selene* section will be 24 m instead of the 40 m used here, while keeping the λ range, one can assume that the chromatic aberration plays in the sub-mm range for the proposed reflectometer with two *Selene* sections [→3.4]. In addition, it affects only the spot size normal to the scattering plane.

1.3.4 length of the guide system

The length of the *Selene* guide system is defined by the total length of the instrument X, the position of the first focal point (in or behind the beam extraction section), and the distance to the detector. The total length X is determined by the λ-range to be covered:

$$X/\,\text{m} \approx 4000\,\frac{T/\,\text{s}}{\Delta\lambda/\,\text{Å}} \tag{1.3.6}$$

with the repetition time $T = 0.07\,\text{s}$.

The sample detector distance is obtained by the needed resolution [→1.5] and is of the order 2 to 8 m.

This leads to a length of the *Selene* section of $4c = 20\,\text{m}$ to 50 m.

1.3.5 technical aspects

quality of the guides
stability
alignment

1.3.6 comparison to a straight guide

A (bent) straight guide accepts a part of the phase space emitted by the source and transfers it to its end. In addition it acts as a filter for short wavelengths and it reduces the intensity due to non-perfect coatings. The definition of the divergence seen by the sample is realised by a slit or a collimator. The beam stays divergent after these elements. This way one selects less than 1% of the neutrons leaving the guide. Neglecting the reduced performance of optical elements, this is the maximum flux one can have on the sample according to Liouville's theorem. So a straight guide has the 2 disadvantages that it delivers much more neutrons than actually needed, and the beam is always divergent so that it over-illuminates the sample and eventually the sample environment.

The inverse approach is to define a maximum beam spot size and divergence required for the instrument. In the next step one has to find an optics and guide geometry that fulfils this requirement, and which avoids all other neutrons, if possible.

For a reflectometer for small samples ($< 10 \times 10\,\text{mm}^2$) one possible solution is the presented *Selene* set-up: The spot-size is chosen with the initial slit (P_1), the maximum divergence is given by the geometry and coating of the elliptic guides.

2.4 experiments on Amor

Selene Amor

2.4.1 Amor

Amor is a neutron reflectometer at SINQ, PSI [**?**], which allows for a wide range of set-ups The scattering geometry is vertical so that liquid surfaces are accessible. Most components are positioned on an optical bench which allows to play with the resolution, or to test exotic set-ups like the prism approach by R. Cubitt [4] or the *Selene* concept. In general Amor is operated in time-of-flight mode (realised by a double chopper), but it is also possible to run it with a monochromator.

The ML-monochromator is placed on the frame-overlap mirror stage and can be driven out of the beam.

The chopper is positioned in a housing, some cm behind the end of the neutron guide. It consists of 2 discs, 490 mm apart, each with 2 openings of 13.6°. In general it is operated in a way to give $\Delta\lambda/\lambda = \text{const.}$[6] For the tests we used a pulse frequency of $23.\bar{3}$ Hz (corresponding to 700 rpm).

The chopper housing limits the maximum incoming divergence because it leads to a minimum distance between the end of the guide to the first diaphragm of 1500 mm, and to the first place where to put a monochromator (on the frame overlap filter stage) it is some 1800 mm.

Behind the chopper housing and the 1st diaphragm a frame overlap filter is mounted. It consists of Si-wafers of 0.6 mm thickness, coated with a Ni/Ti $m^f = 2$ SM. If placed in the beam with an inclination of θ^f it reflects all neutrons with $\lambda > 4\pi \sin\theta^f / m^f q_{\text{Ni}}^c$. In the case of the strongly divergent beam the deviation of α^f from θ^f has to be taken into account. The cut-off wavelength is then $\lambda^f = 4\pi \sin(\theta^f - \theta)/m^f q_{\text{Ni}}^c$.

In TOF mode (without monochromator) the situation is more complicated: All neutrons trajectories accepted by the elliptic guide should provide all required wavelengths. But the flat frame-overlap filter acts angle dependent. A possible solution is to build a filter bent accordingly [→B.4]. This then is optimised for one specific cut-off wavelength.

2.4.2 high intensity specular reflectometry

A principle sketch of this mode is given in A.1. The standard disc choppers of Amor were used, operated at 750 rpm, giving a pulse rate of $25\,\text{s}^{-1}$. The first slit after the chopper housing was used to define the initial beam size. All other slits were removed or driven out of the way. The distance from the sample position to the detector was 3000 mm. No frame-overlap filter was installed.

The samples were (a) a $[\text{La}_{1/3}\,\text{Ca}_{2/3}\,\text{Mn}\,\text{O}_3\,/\,\text{Y}\,\text{Ba}\,\text{Cu}\,\text{O}_3]_5$ multilayer on $\text{Sr}\,\text{Ti}\,\text{O}_3$ with a period of 600 Å and a layer thickness ratio of 2 : 1. As reference to normalise the measurements and to characterise the beam (b) a NiTi supermirror with $m = 5$ was used. Both samples had a surface area of $10 \times 10\,\text{mm}^2$.

Figure 2.12 shows the intensity maps $I(\lambda, \theta)$ for both samples, and for the re-normalised map. The reflectivity extracted there from is displayed in figure 2.13. The measurement times for the maps shown were 4 h, each, at an angle $\omega = 1.5°$. The same measurements were performed also in 24 min and in 2.5 min, and at higher angles.

In map 2.12 (a) the iso-q_z lines for the first, second and fourth Bragg peak and for the total reflection edge are nicely visible. The dark line at $\theta \approx 0.9°$ originates from a mis-alignment of the guides. This just leads to a reduced intensity, not to systematic errors. Since these measurements and the data reduction were performed with a constant $\Delta\lambda \propto \Delta t$ while the instrument has a resolution $\Delta\lambda/\lambda = \text{const.}$, the resolution at low q_z is underestimated, and at high q_z a coarser binning could be performed without loss of information, which would qualify the error-bars.

fixed values	/ mm
guide end – chopper housing start	: 75
guide end – chopper housing end	: 1309
guide end – earliest position polariser	: 2744
1st slit – earliest position polariser	: 1242
typical values	
chopper disc 1 – chopper disc 2	: 490
3rd slit – sample	: 400
sample – 4th slit	: 400

Table 2.1: List of typical or fixed distances on Amor.

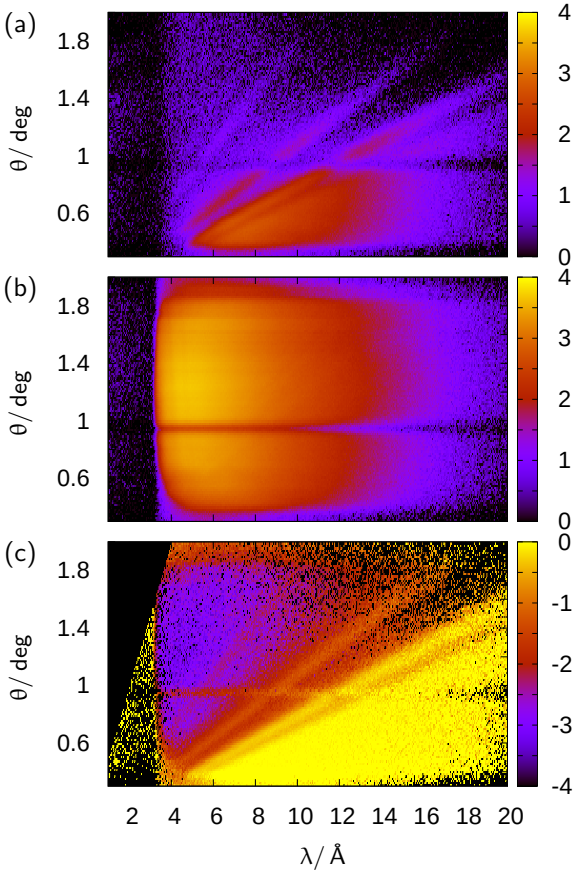

Figure 2.12: Intensity maps $\log_{10}[I(\lambda, \theta)]$ measured in 4 h with a LCMO/YBCO multilayer (a), and a NiTi supermirror (b). From these map (c) is obtained by division. (d, blue line) Reflectivity curves $R(q_z)$ obtained by summation over equal q_z of the map (c). The red and green lines correspond to counting times of 24 min and 2.5 min. The differences visible at $q_z \approx 0.3\,\text{Å}^{-1}$ originate form a not yet correct treatment of the errors of zero-count channels.

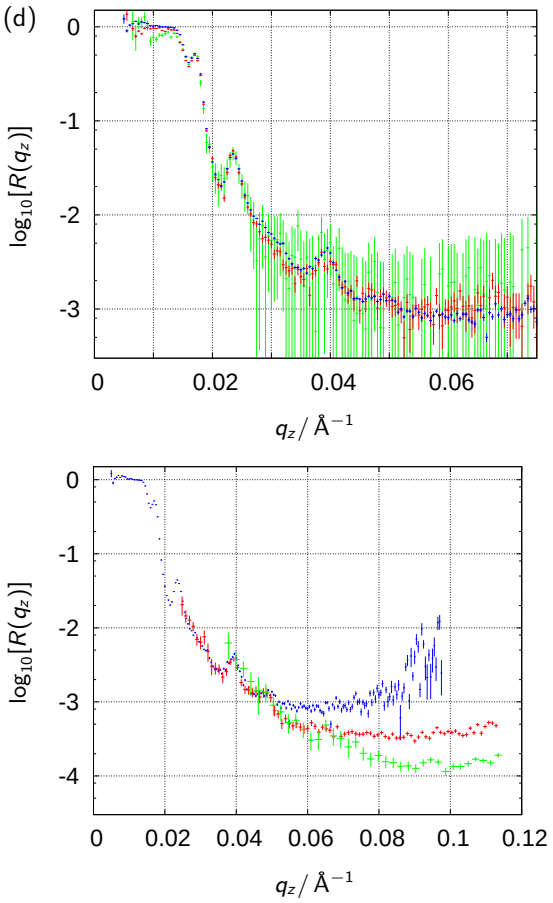

Figure 2.13: Reflectivity of a LCMO/YBCO multilayer. The blue curve is identical to the one in figure 2.12 (d), the others were obtained in a similar way with $\omega = 3°$ (red), and $\omega = 4°$ (green). The resolution was reduced accordingly. The deviations clearly illustrate the influence of the λ-dependent background.

The fact that $R(q_z)$ reaches the background at 10^{-3}, already, has two reasons: No frame-overlap filter was used, so that the totally reflected neutrons with $\lambda > 24\,\text{Å}$ leak in at nominally $\lambda > 4\,\text{Å}$. This leaking can be seen in the maps at $\lambda < 3.5\,\text{Å}$. And more severe, the instrument background is highest for $\lambda \approx 5\,\text{Å}$. This is visible in map (a) for $\theta > 1.8°$. In principle this can be suppressed, but the improvised set-up and the horizontal offset of the beam prevented the usage of the slits and shielding material available on Amor. Both problems will be solved for the next beamtime.

2.4.3 angle-wavelength encoding

In addition to the operation mode described in 2.4.2 a multilayer monochromator (→ 2.2.4) is installed after the chopper. As a consequence the first slit on Amor could not be used anymore and was replaced by a manual slit system behind the monochromator. Unfortunately, the chopper was operated at 1500 rpm and with a non-adequate time binning scheme. This results in half the intensity for $\lambda < 6.8\,\text{Å}$. The samples where

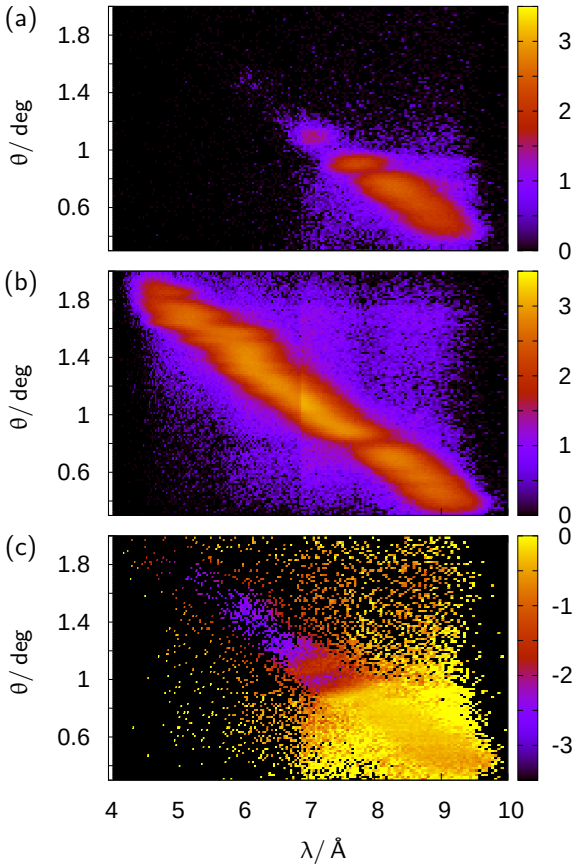

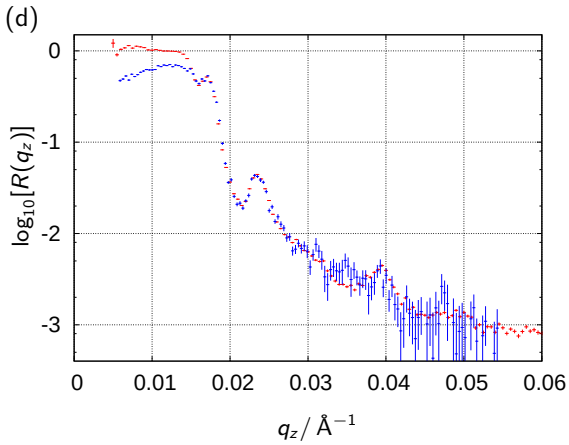

Figure 2.14: Intensity maps $\log_{10}[I(\lambda, \theta)]$ measured in 4 h with a LCMO/YBCO multilayer (a), and a NiTi supermirror (b). From these map (c) is obtained by division. (d, blue line) Reflectivity curve $R(q_z)$ obtained by summation over equal q_z of the map (c). The red line is identical to the blue on in figure 2.12 (d).

the same LCMO/YBCO multilayer and NiTi supermirror discussed above.

The resulting reflectivity is compared to the one obtained with the height-intensity mode in figure 2.14 (d). The much reduced statistics displays the intensity gain one gets by loosening the resolution and using a high divergence. In addition for $q_z > 0.03\,\text{Å}^{-1}$ the mentioned mismatch of chopper speed and time binning leads to a further reduction of the statistics by a factor 2.

The deviation of $R(q_z)$ for small $q - z$ results from problems with the normalisation. Most likely the positions of both samples where not exactly identical, leading to a slightly different illumination. This is most severe for low angles, where the projected sample size might be smaller than the position off-set.

2.4.4 discussion

Overall the test series on Amor was successful, for it proved that even delicate samples can be measured. The gain in counting time relative to the normal operation mode on Amor is about one order of magnitude for small samples. This value was estimated from the actual counting time, the illuminated sample area, and the difference of the chopper speeds.

The measurements also revealed the problems still present. The different beam geometry requires adapted shielding and modified slit mounts to reduce background. This was already realised by end 2012.

The horizontal stripe pattern visible in the intensity maps results from a misalignment of the guide elements and from waviness on the reflecting surfaces. The relative alignment of the guides can be improved. Mechanical modifications are being discussed with SwissNeutronics. For the waviness the problem is more difficult to solve. We found area on the surface, almost free of detectable waviness, and area with severe deviations. It is planned to investigate this qualitatively and to find solutions together with SwissNeutronics. The waviness leads to distortions in the angle-wavelength encoding and thus to a reduced resolution in this operation mode. For the other modes it just results in a reduction of the intensity by fractions of a percent, so it might be neglected there.

The small sample size together with the small beam spot requests a more precise and reproducible way to align the sample. Here we want to investigate approaches as used in x-ray or synchrotron experiments. The challenge will be to realise these when using e.g. a cryomagnet.

To suppress the frame-overlap, a bent transmission filter according to section B.4 will be constructed and build.

Further tests on Amor are scheduled for May 2013.

3 instrument for small samples

ESS*Selene* small samples

The leading design task for this instrument is to be able to perform reflectometry on *small samples*. I.e. the flux and the pulse structure of the ESS are mainly used to achieve this goal. The instruments optimisation towards other criteria like high q_z range, time resolved measurements, polarisation, and so on, should not affect (severely) the leading task.

Small here means surface area 1 or 2 orders of magnitude smaller than presently possible (as a standard method). We aim for a footprint size from $10 \times 10\,\mathrm{mm}^2$ (state-of-the-art) down to $0.3 \times 0.3\,\mathrm{mm}^2$. This is optimal for samples who's (homogeneous) size is restricted by the preparation method to below $1\,\mathrm{cm}^2$, e.g. PLD-grown metal-oxide heterostructures. Bent or curved surfaces become accessible because the beam footprint can be restricted to a small area and thus the angular resolution is hardly affected. Inhomogeneous samples can be scanned, e.g. to avoid areas with damages, non-perfect coating, or gas bubbles in liquid/solid cells.

The instrument is flexible enough to measure all kinds of samples besides liquid/liquid or liquid/gas interfaces. The wide free space around the sample position allows for bulky sample environment, and for simultaneous usage of complementary techniques.

The *Selene* guide on a pulsed source allows for the combination of the angle-dispersive and the energy0-dispersive operation modes of classical reflectometers: for each moment (i.e. wavelength) a scan across the detector corresponds to an angle-resolved measurement, and at each position on the detector one gets a TOF reflectivity measurement. The resulting time-dependent phase-space can be modulated in a way to allow for almost conventional TOF, selectable constant resolution from 3% to 20%, high-intensity specular reflectometry, etc. So it is possible to screen some parameters within a short time, and then to perform high-quality measurements with optimised conditions. Also time-resolved investigations on the second-range are possible.

The small footprints set high limits for the quality of the guides and the possibility to align them. Since the focal spot size is given solely by the initial slit size, the de-tuning of the two guides (sections A.5 and A.4) and the surface fidelity of the guide, there is no possibility to reduce the beam spot with slits after the end of the guide system.

Since for very small samples it will still be difficult to reach high q_z or large dynamic ranges, the option of a full-convergent beam geometry (A.1) is ideally suited for this application.

The need to reduce background and to increase radiation safety might lead to more shielding than given in the ESS baseline (6 m radius for the monolith), or as mentioned at IKON3 (12 m radius, no line of sight, no line of sight to directly irradiated area). Since the *Selene* guide systems implies an *early* manipulation of the beam, the geometrical situation and the accessibility of the *early* region of the beamline strongly affects the instrument lay-out. Thus the options and parameters given in the following sections can not be final, but they reflect the actual state of the work.

3.1 science case

Typical small samples are hard matter herterosructures where the production process limits the (homogeneous) are to below 1 cm^2. This is e.g. the case for layered metal oxide films grown by pulsed laser deposition (PLD).

...

The need to reach high q_z and thus high detector angles (up to 46° for $q_z = 1\,\text{Å}^{-1}$, 106° for $q_z = 2\,\text{Å}^{-1}$) favours a horizontal scattering geometry. This is also supported by the fact that than gravity affects the beam profile and divergence only in the sample plane.

The only restriction caused by the vertical sample plane is that liquid/gas and liquid/liquid interfaces can not be studied.

magnetic metallic or oxidic heterostructures This group of materials are the main target for the small samples reflectometer. Depending on the materials involved the samples are grown by pulsed laser deposition (PLD), sputtering, molecular beam epitaxy (MBE), or the like. Especially PLD-grown samples often suffer from the inhomogeneous thickness of the film for areas larger than $5 \times 5\,\text{mm}^2$. The homogeneity is important not only for the reflectometry measurements, but also it often determines the properties of the film. E.g. the sign of magnetic coupling through a non-magnetic spacer layer might change as a function of the spacers thickness.

A widely used substrate for perovskite-type heterostructure is $SrTiO_3$, which upon cooling undergoes several phase transitions. The one at 105 K leads to a twinning and as a consequence to a fragmentation of the surface, where the individual facets reflect in different directions. With a small footprint one can reduce the number of active facets for measurements.

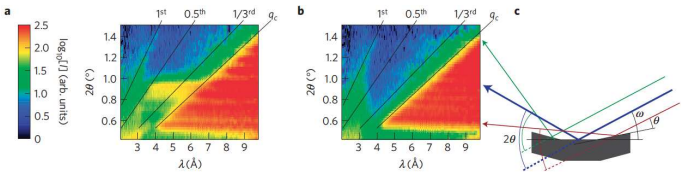

Reflectivity measured on a curved sample surface with a highly collimated incoming beam. The individual facets of the surface correspond to the steaks with θ = const.. [?]

Samples investigated with synchrotron radiation methods often are below 1 cm^2 to fit in the HV sample environment. The presented instrument would be able to investigate the same samples for complementary information. E.g. in combination with XRD, XMCD and resonant x-ray reflectometry.

Samples showing eclectic effects (polarisation, multiferroic properties) often need to be conducted. A focused beam then allows to measure in a region without contacts to avoid uncontrolled absorption, background and eventually phase shifts in part of the reflected neutrons (e.g. contact/film interface instead of vacuum/film).

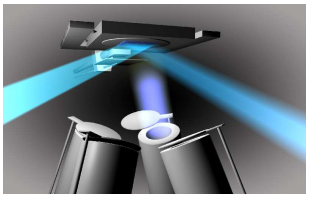

non-magnetic metallic or oxidic heterostructures

soft matter films and heterostructures on a substrate Since samples of this type often can be produced with surface area of 10 cm^2 to 100 cm^2 they would profit from a footprint width larger than $\approx$ 1 cm. Nevertheless they can be investigated on this instrument.

... rare substances ....

... expensive material ....

liquid/solid interfaces Liquid/solid cells can be mounted and measured without problem. Since the footprint can be defined exactly way before the sample it is possible to avoid the illumination of the gasket and the liquid vessel. Again, for larger cells the width of the footprint might be less than acceptable by the sample. On the other side one can even reduce the footprint to scan the interface for inhomogeneities (e.g. non-perfect coating or air bubbles).

laterally structured surfaces For these it is essential to measure the off-specular reflected signal. This is possible by using a slit directly after the guide (2.4 m or 4.5 m form the sample) which leads to an almost conventional TOF reflectometry set-up. "Almost" means that the beam is still convergent! The slit just defines the θ-range, not the footprint size. Moving the slit between pulses allows to vary θ without rocking the sample.

non-perfect surfaces

GISANS The focused beam in principle allows for focused GISANS experiments. The area detector has to be put in the focal plane, the sample as far away as possible, i.e. close to the end of the guide. Without sample the beam spot on the detector is defined by the initial slit, its divergence by the guide, eventually reduced to fit the sample size.

A laterally structured sample, mounted in the convergent beam leads to scattering and diffraction.....

It is not yet clear if the beam leaving the guide is clean enough for high-quality GISANS measurements. Also the sample-detector distance of 2.4 m or 4.5 m is rather small and requires a high spacial resolution of the detector. On the other side one can use the full convergent beam, unlike when multi-channel collimators are used behind a guide with divergent beam.

spin-echo techniques In cooperation with Robert Georgii and Wolfgang Häußler, both from the Technical University Munich, we investigate the possibility to have a MIEZE set-up as an add-on. The second coil could be installed in the space before the sample, the first one in an equivalent position before the a guide element. This way all trajectories between the coils are of the same length. ($\rightarrow$ **??**)

The space before and behind the sample would also allow for the installation of a SERGIS set-up.

3.2 boundary conditions and consequences

Based on information distributed at IKON3, and on private communications with P. Bentley, K. Anderson, and H. Wacklin, 11. 2012, there are the following boundary conditions to be expected for a *short* reflectometer. Short means of the order of 50 m long or less, i.e. situated in one of the inner guide halls at the ESS.

3.2.1 space

- The first 2 m around the moderator are free of any elements.
- Within the target monolith shielding (2 to 6 m) an insert of horizontally a 5° wedge, but less that 210 mm, and vertically of 210 mm can be freely shaped. Optical elements are allowed in the insert. Since there will be a cooled He atmosphere (from moderator up to the end of the monolith) also free-standing Si-wavers can be used.

  The last 500 mm of the monolith might be occupied by a shutter (which can host optical elements).
- Behind the monolith there might be a chopper or other moving parts.

- From the monolith up to a radius of 15 m a common shielding for all instruments will be build. The beam guide can be of any shape and size. There is the option to insert choppers and other devices (most likely accessible from top).
- At a distance larger than 15 m to the moderator, the individual instrument guide shielding starts. Its length depends on the dose rate caused mainly by fast neutrons (also by secondary processes).
- The *short* instruments will have a 10° wedge-shaped space available. This is necessary to allow for sufficient shielding to prevent cross-talk of background.
- The height differences from moderator to floor are 3 m and 2 m. The hall allowing for high magnetic fields will have the 2 m distance. If needed it is possible to get a lower floor locally.

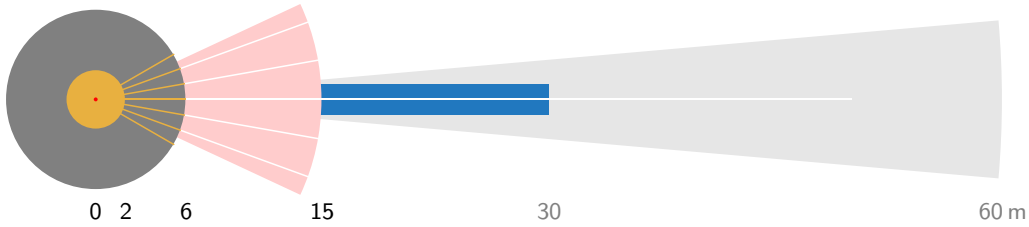

Figure 3.1: Sketch to illustrate the various shielding jackets intended for the source and the instrument. The colours mean: red–moderator, yellow–He-atmosphere, gray–target-shielding, light red–common instrument shielding, blue–individual guide-shielding (as far as possible), light gray–10° wedge available for a short instrument.

3.2.2 shielding and background

- The target monolith (for the moment) is intended to consist of steel.
- The common instrument shielding will be made of various materials to moderate fast neutrons, convert muons and neutrons, and absorb γ and neutrons.
- The effective direct line of sight from any point of the instrument area to the moderator and target is to be avoided. This means at least 12 m material in the direct line.

  At most half of the length of the guide (shielding) is to have direct line of sight.
- Indirect line of sight has to be avoided. I.e. from outside the shielding no area directly illuminated by the source (moderator and target) is visible. Here the thickness of the shielding material is about 2 m?

U. Filges made MCNPX calculations for a reference shielding, which does not fulfil the mentioned criteria. It is made of steel, only, and allows for a direct line of sight from sample (detector) to the moderator. !!!

Based on these constrains it might be favourable to substitute the one *Selene* guide section as discussed in section **??** for two identical sections of half the lengths. Direct line of sight is blocked much earlier and the joining focal point is in an environment of low radiation allowing for easy access. The two versions are discussed in sections 3.3 and 3.4.

3.2.3 exclusion of proton prompt

At ISIS second target station and at the SNS the fast neutrons and hard x-rays produced during the proton pulses (or by secondary processes in the shielding) cause problems in the data acquisition. The corresponding STAP members R. Dalgliesh and J. Ankner suggest not to collect data during these times. So it is favourable to tune the instrument length and λ-range in a way to exclude the pulse times without creating holes in the q-range.

For the time being all reflectometers should be developed in a way that the time interval of high fast neutron background is excluded from the measurements.

Following the argumentation of section 1.1.1 the usable wavelength range for reflectometry starts at about 4 Å to 5 Å for *Selene* guides. An instrument length of some 60 m results in a wavelength range of e.g. $\lambda \in [5, 10]$ Å.

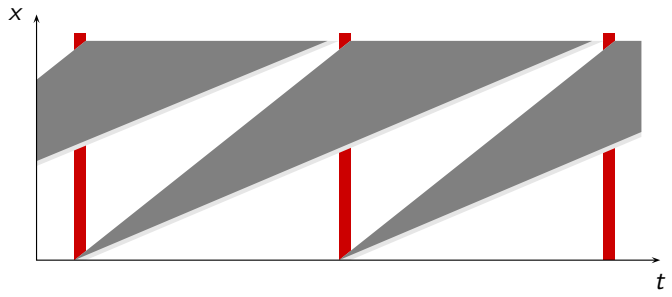

Figure 3.2: Sketch to illustrate how to avoid the influence of the γ and fast neutron burst from the proton pulse hitting the target. The sketch is to scale with period $T = 70\,\text{ms}$, pulse length $t = 3\,\text{ms}$, and a sample detector distance of 58 m, i.e. $\lambda \in [5, 9.3]\,\text{Å}$.

For the ESS baseline parameters this has the consequence that the background burst from the proton pulse appears at the be beginning or the end of the used wavelength range. Further optimisation leads to the situation that the bursts are just outside the required λ range, as is sketched in figure 3.2.

For this scheme, the flight times for the shortest / longest wavelength are $t = 73\,\text{ms}$ / 137 ms (assuming a burst time of 3 ms and a period of 70 ms). For $\lambda_{\text{min}} = 5.00\,\text{Å}$ this leads to an instrument length of $\overline{SD} = 58'400\,\text{mm}$, and this in turn to $\lambda_{\text{max}} = 9.38\,\text{Å}$.

The intrinsic λ resolution for this instrument is then

$$\begin{aligned} \Delta\lambda/\lambda &= \Delta t/t \\ &= \tau/t \\ &= 3.8\% \ldots 2.1\% \text{ for } \lambda = 5\,\text{Å} \ldots 9.4\,\text{Å} \end{aligned}$$

3.2.4 technical limitations

3.4 double-Selene guide system

This is an alternative approach to the one discussed above (3.3), paying respect to much higher shielding demands. If the target monolith and the shielding around the first guide are not sufficient (as is claimed by the experts from ISIS and SNS), one can build a guide system with 2 subsequent *Selene* sections. The first looks on a fix pin hole in the extraction section and creates a small but homogeneous virtual source some 20 m to 30 m from the moderator. From there direct and first indirect line of sight is blocked efficiently. The beam is then manipulated (shaped, polarised, filtered) at or close to that virtual source point and fed into the second *Selene* guide system.

The considerations for the instrument length are the same as in (3.3), but the divergences can be chosen more flexibly since the aperture defining the virtual source at the first focal point does not need to be manipulated and can be located anywhere in the target monolith (after 2 m from the moderator). Tables 3.3 and 3.4 give the parameters of the instrument and guide, and figure 3.6 shows a possible realisation.

Using two *Selene* sections has the result, that the guide dimensions are reduced by a factor 2, gravity effects are reduced by a factor 4, but the number of reflections in the guide increases from 4 to 8. This means that this approach favours longer wavelengths where the reflectivity of the coating is more efficient.

Table 3.3: Physical parameters and properties of the reflectometer for small samples using two subsequent *Selene*-type guides.

parameter space		
q_z-range	$[0, 1]\,\text{Å}^{-1}$	to be covered in 5 measurements
λ-range	$[5, 9.3]\,\text{Å}$	
sample size	$[0.3, 10] \times [0.3, 10]\,\text{mm}^2$	
maximum divergence	$\Delta\theta_{xy} = 1.5°$	scattering plane
	$\Delta\theta_{xz} = 1.5°$	sample plane
resolution		
intrinsic $\Delta\lambda/\lambda$	2.1%	5.0 Å
	4.0%	9.4 Å
$\Delta q/q$ = constant	3%, 5%, 10%, ...	with multilayer monochromator
moderator	cold	
geometry		
scattering plane	horizontal	
total length	58.0 m	
moderator / end of shielding	26.0 m	
end of guide / sample	2.4 m	
sample / detector	6.2 m	
2θ	−2° to 50° (110°)	for $q_z \leq 1\,\text{Å}^{-1}$ ($2\,\text{Å}^{-1}$)
guide transmission	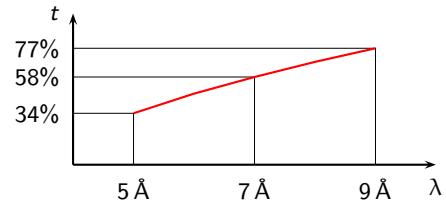	analytical, based on eqn. 1.1.2
detector		
angular width	2.8° × 4.5°	vertical × horizontal
angular resolution	0.005°	
size	300 × 500 mm²	for 6.2 m distance to sample
pixel size	0.5 × 0.5 mm²	"
options		
polarisation & analysis		
sample environment	cryo-magnet	
add-on	MIEZE, SERGIS	

λ	t
5 Å	34%
6 Å	47%
7 Å	58%
8 Å	68%
9 Å	77%

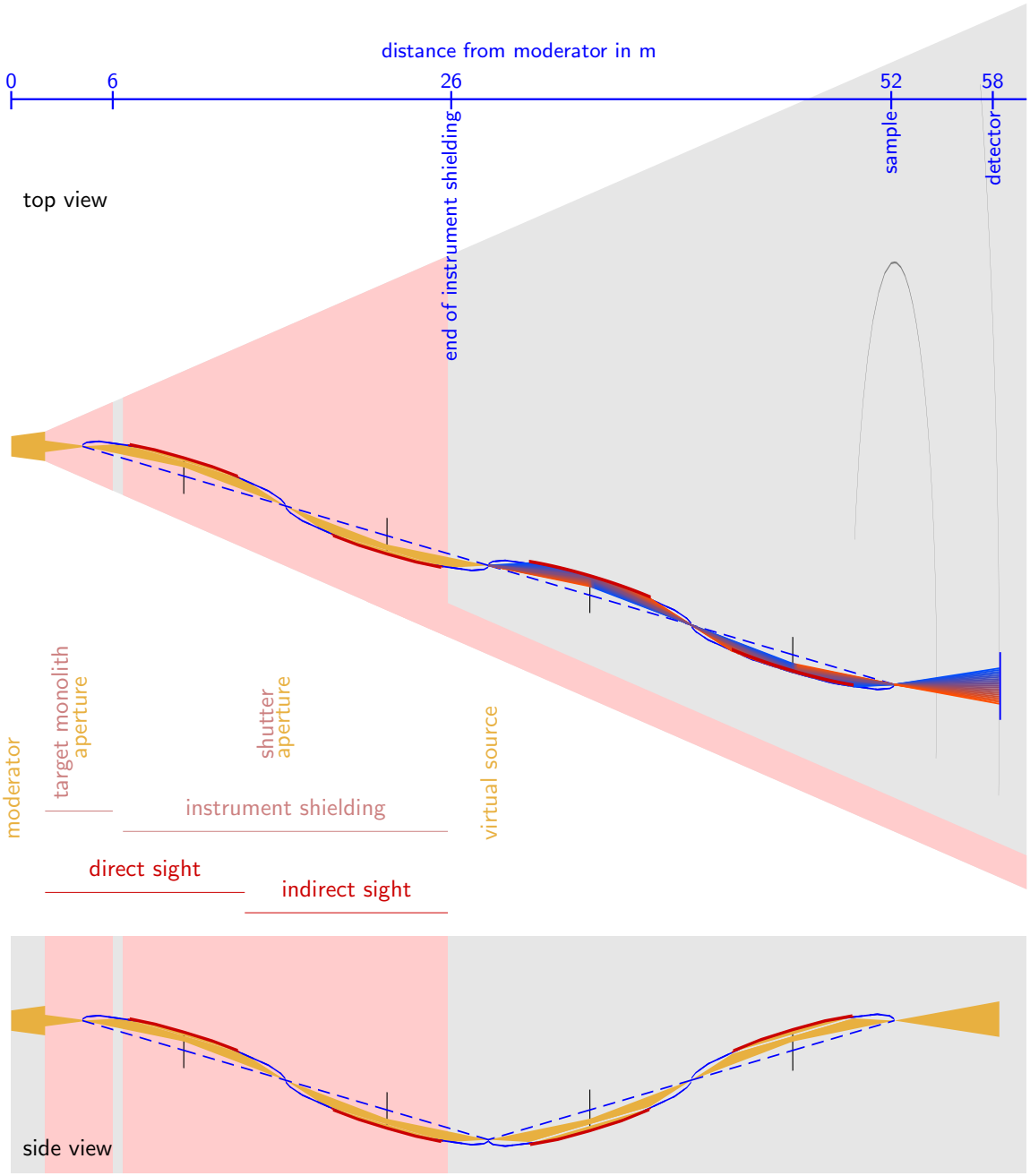

Figure 3.6: Sketch of a guide system with two subsequent pairs of ellipses. A small ($10 \times 10\,\mathrm{mm}^2$) aperture 4.2 m from the source acts as the initial focal slit for the first *Selene* guides. These are completely within a shielding. Direct line of sight to the source is possible all along the first guide element. Secondary radiation can be directly seen all along the second guide element. Behind that the beam is focused down to the size of the initial aperture. At that point the precision shaping of the footprint is performed. The second *Selene* guide acts as in the set-up described above. This way the shielding ends some 26 m after the moderator. The beam channel is bent several times so that the radiation level should be much reduced. The polariser or a band-pass filter will be positioned in a low-radiation region easily accessible for maintenance.

Table 3.4: Parameters of the *Selene*-type guide. For a given instrument length of 58 m and $\Delta\theta_{xy} = \Delta\theta_{xz} = 1.5^\circ$ the following guide parameters are obtained bu analytical calculations. For the beam extraction see also (1.2.4).

guide parameters		
c	6.0 m	
ξ	0.6	
b/a	0.01754	$\Rightarrow \quad b = 105.26\,\text{mm}, \quad a = 6000.92\,\text{mm}$
coating	$m = 2.5$	
distances		
moderator / pin hole	4.2 m	first focal point
$2c$	12.0 m	length of ellipses
$\xi \cdot 2c$	7.2 m	length of (coated) guide sections
$(1-\xi) \cdot 2c$	4.8 m	space between guides
$(1-\xi) \cdot c$	2.4 m	space before sample
sample / detector	[1.5 . . . 7.5] m	high-angle diffraction vs. high resolution
Δz at P_3	522.7 mm	vertical offset of one *Selene* section
Δy at P_3	522.7 mm	horizontal offset of one *Selene* section
free space for chopper locations (distance from the moderator)		
6.0 m → 6.6 m		
13.8 m → 18.6 m		
25.8 m → 30.6 m		
37.8 m → 42.6 m		
49.8 m → sample		
q_z ranges for one angular setting		
θ_{min}	q_z range	
0.4°	0.01 Å^{-1} → 0.08 Å^{-1}	
3.0°	0.07 Å^{-1} → 0.19 Å^{-1}	
7.7°	0.18 Å^{-1} → 0.38 Å^{-1}	
16.0°	0.37 Å^{-1} → 0.72 Å^{-1}	

3.4.1 simulations

The simulations were performed with McStas [7, 8]. For the time being, gravity is not taken into account for the extensive simulations with samples. The reason is that the tapered guide component which can handle gravity gets too slow when used with a sufficiently high spatial resolution. Also there is no real polarisation performed. Instead two simulations with varying SLD for the magnetic material are run. And off-specular scattering from any element is not yet taken into account.

instrument file The instrument file consists of standard `Slit` components mimicking the extraction unit with pin-hole, the `Guide_four_side` component for the *Selene* guide elements, and a `Mirror` component for the sample. The detector is a monitor of the type `Monitor_nD`, collecting location on the detector and time-of-flight in single event mode. A representative instrument file is given in D.2.

The guide geometry, the distances and the coating are the ones given in figure 3.6, and in tables 3.3, 3.4. For the moment the raw data are binned to $\Delta y = \Delta z = 0.5\,\text{mm}$ on the detector, and to $t_n = t_0 * 1.005^n$ in time.

high-intensity specular reflectometry, natural resolution For this simulations the bare double *Selene* guide is used, without any slits or other optics to tune the angular resolution, and without chopper to shape the pulse. The λ resolution is thus $\Delta\lambda/\lambda = \tau/t$ and ranges from 2.1% to 4.1% within the λ range..

Figure 3.9 shows intensity maps $\log_{10}[\,I(\lambda,\theta)\,]$ for 4 orientations of the multilayer $[\text{Ni}(120\,\text{Å})/\text{Ti}(80\,\text{Å})]_{20}/\text{Si}$, $\sigma = 4\,\text{Å}$ with a surface area of $10 \times 10\,\text{mm}^2$ [→D.1]. The normalisation of the *measurement* was performed by using an ideally reflecting sample of the same shape.

The ω and thus the θ ranges were chosen so that some overlap in q_z is realised. This can be seen by following the bright (iso-q_z) kines in the gray-shaded area. From the map it is also apparent that the statistics for lowest and highest q_z for one ω is reduced, because the corresponding area in the lower right and the upper left corner are relatively small.

From these maps the specular reflectivity shown in figure 3.9 were obtained by integration along constant q_z. The resolution $\Delta q/q$ varies over the $I(\lambda,\theta)$ map and with ω. Thus the $R(q_z)$ curves have a complicated non-Gaussian resolution function [→C.3.1]. Nevertheless the agreement with the red curve with a 2% resolution is quite good. The essential deviations are the depth of the minimum around $q_z \approx 0.06\,\text{Å}$ and the peak heights

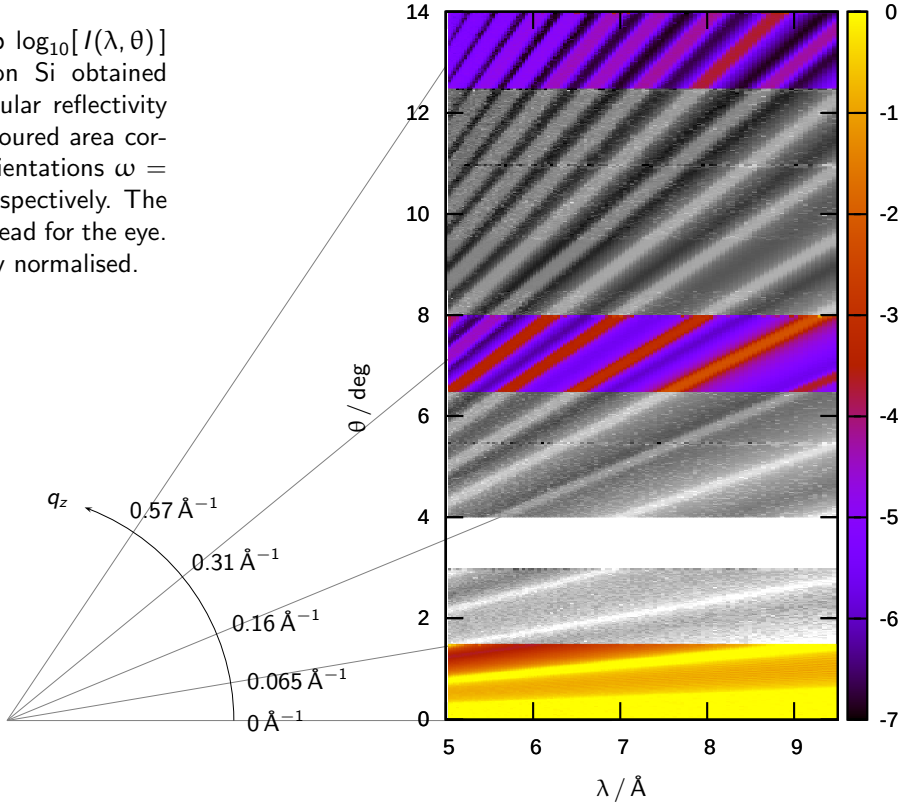

Figure 3.7: Intensity map $\log_{10}[\,I(\lambda,\theta)\,]$ for a Ni/Ti multilayer on Si obtained in the high-intensity specular reflectivity mode [→A.1]. The 4 coloured area correspond to the sample orientations $\omega = -0, 5°$, 2°, 6°, and 12°, respectively. The gray-scale area are just a lead for the eye. The intensities are already normalised.

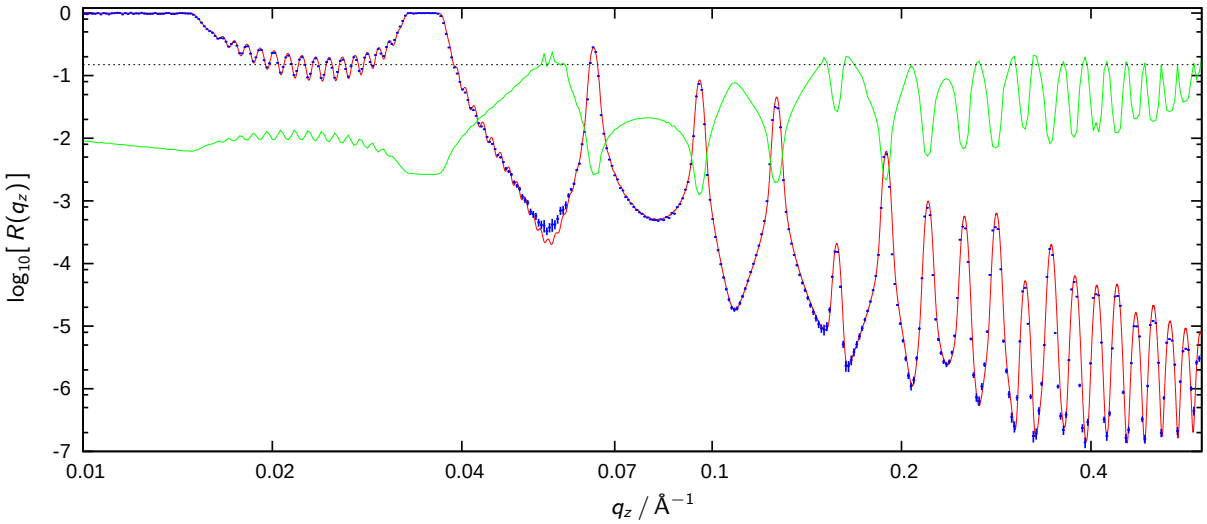

Figure 3.8: $\log_{10}[R(q_z)]$ of a Ni/Ti multilayer on Si. The sample size was $10 \times 10\,\mathrm{mm}^2$. The red curve corresponds to the coating of the sample, convoluted with $\Delta q/q = 0.02$. In blue the *measured* signal is given on a grid with $\Delta q/q = 0.01$. The green curve gives the corresponding relative error for *counting times* of 2 s, 20 s, 60 s, and 240 s for the sample orientations $\omega = -0,5°$, 2°, 6°, and 12°, respectively. These times were obtained by restricting the relative error to below 0.014 (black dots).

for high q_z. If this can be improved by more intelligent binning, integration and convolution with a correcting resolution function [→C.3.2] has to be investigated.

The pure counting time sums to 5.5 min. Including the expected positioning times for the detector the measurement can be realised within 7 min.

> The simulation does not really give intensities, but expectation values for the intensity collected in 1 s. To estimate the statistical error one can assume $\Delta I(\lambda,\theta,t) \approx \sqrt{I(\lambda,\theta,t)}$ with $I(\lambda,\theta,t) = I(\lambda,\theta)\,t$ where t here is the virtual counting time. The relative error thus behaves like
>
> $$\frac{\Delta I(\lambda,\theta,t)}{I(\lambda,\theta,t)} = \frac{1}{\sqrt{I(\lambda,\theta)}}\,\frac{1}{\sqrt{t}}$$
>
> The minimum $I(\lambda,\theta)$ together with the constraint of a maximum allowed relative error thus gives the minimum counting time. Here at least 50 counts per channel were assumed leading to a relative error of maximum 14%.

λ/θ encoding At the focal point in between the two *Selene* guide sections of the instrument model used above, a NiTi multilayer with a peak at $m = 3.4$ was added, and the second *Selene* section was tilted accordingly. The intensity maps obtained this way look qualitatively the same as the one shown in figure 3.4 (a).

For extracting the reflectivity curves from the intensity maps two aproaches were followed. The first is identical to the data reduction for the high-intensity specular reflectivity. I.e. the integration is performed over the full λ-θ area, assuming that the intensity in the off-specular radiation caused by the finite reflectivity of the monochromator for $m \neq 3.4$ can be neglected. The second approach restricted the integration to an intervall $\lambda \in [\lambda(\theta) \pm \Delta\lambda]$, with $\lambda(\theta) = 4\pi\sin(\omega_m + \omega - \theta)/m\,q_{Ni}$, and $\Delta\lambda$ defined by the time-resolution τ. For both approaches the corresponding $\log_{10}[I(\lambda, q_z)]$ maps are shown in figure **??**.

Since off-specular reflectivity of the monochromator is not yet included in the simulations, both approaches give the same reflectivity curves. The difference in statistics is below the % level and thus negligible. The reflectivities are almost congruent with the ones obtained with the ones mentioned above. The only visible difference is that the minimum at $q_z \approx 0.06$ Å is now reproduced correctly.

The difference in counting time for $\omega = -0.5°$ is $t = 100$ s for encoding relative to $t = 2$ s for the high-intensity mode for the same counting statistics.

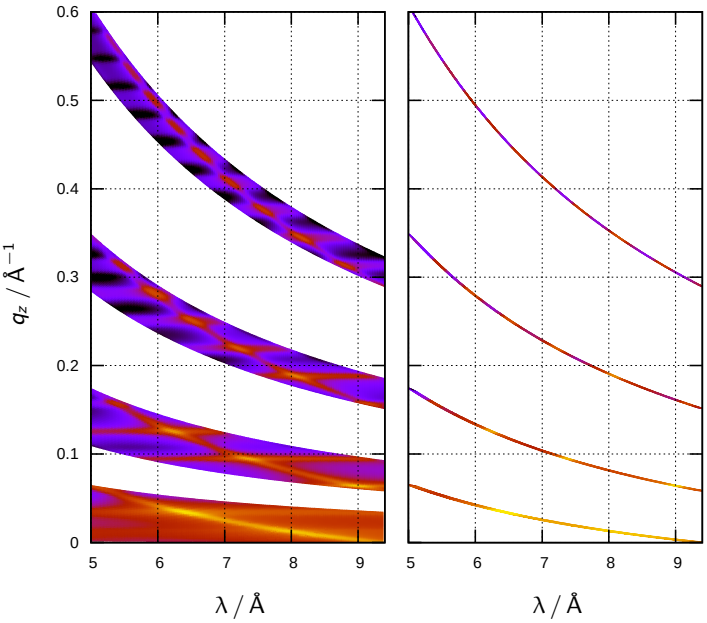

Figure 3.9: Intensity map $\log_{10}[I(\lambda,\theta)]$ for a Ni/Ti multilayer on Si obtained in the λ/θ encoding mode [→A.3]. The 4 areas correspond to the sample orientations $\omega = -0,5°$, 2°, 6°, and 12°, respectively. The intensities are not normalised. The left maps shows the signal after transformation of t to λ and θ to q_z. In the maps on the right side the areas where only off-specular intensity is expected (assuming a perfect monochromator) are shaded.

next steps The almost conventional mode is missing. This will be included within the next days.

To benefit from the simulations (relative to analytical calculations), real effects have to be included. This means over all off-spacular or incoherent scattering form optics and sample, and non-ideal surface orientations (mis-alignment and waviness). Once these topics are included and investigated, the reference samples and conditions proposed by the STAP will be worked on.

3.4.2 benchmarking

3.4.3 shielding

Figure 3.10 shows the shielding concept for the first *Selene* guide section including the target monolith. The extraction unit consists of some highly γ and neutron absorbing material (e.g. tungsten) and leaves only a pin-hole of $10 \times 10\,\mathrm{mm}^2$ at 4 200 mm from the moderator. Behind the monolith there is a gap of 600 mm until the first guide starts. This gap can be used for filters, shutters or choppers. The first and second guide elements ares enclosed in a heavy concrete block. In the sketch at least 50 mm free space between guide and shielding are assumed for support, alignment devices, and vacuum housing. Because the dimensions of the openings are about 3 times the actual guide width, additional shielding is needed before and after the concrete shielding. These masks are displayed in blue. The area directly irradiated from target and moderator ends at the exit of the first concrete block at 13 800 mm. The indirectly irradiated area ends at 25 800 mm, i.e. less than half way between source and detector. Additional shielding and choppers or shutters can be installed in between the guide elements.

The support system for the guides needs more space than just the $160 \times 160\,\mathrm{mm}^2$ within the channel. Swiss-Neutronics suggested to use a granite beam to support the guide. This could also be part of the shielding, with appropriate shape to prevent straight holes parallel to the channel. If granite is suited for this purpose has to be investigated. On the other side one could use a heavy concrete beam as support, if it is stable enough, also against thermal influences.

The second *Selene* guide section will need some shielding, too, but since neither thermal or fast neutrons, nor γ should be in there, only a moderate boron-based absorber should be sufficient. To ensure the absence of fast neutrons, a sapphire filter can be inserted behind the concrete shielding.

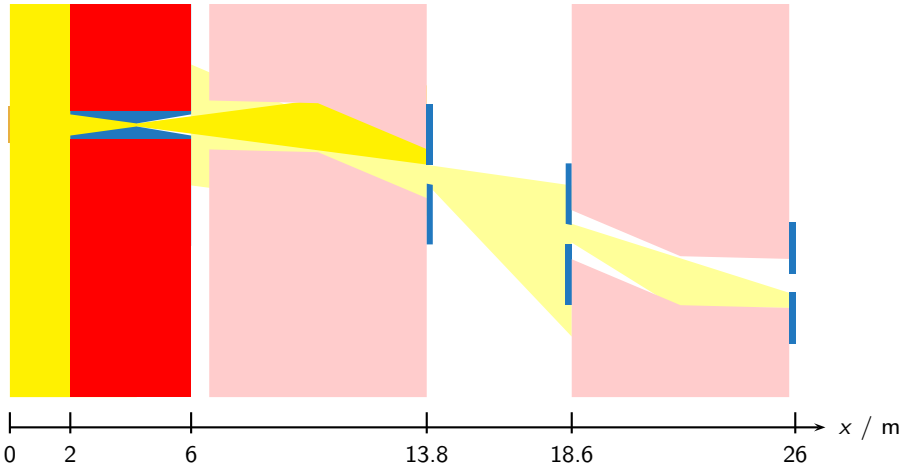

Figure 3.10: Sketch of the fast neutron and γ shielding concept. Here a vertical cut through the shielding is shown, following the beam in horizontal direction. The guide geometry and thus the shielding is the same horizontally and vertically. The source (moderator) is represented by the brown rectangle on the left. The red area stands for the monolith, the blue insert is the extraction unit. The pale red area represent heavy concrete shielding (or a sandwich of various moderators and absorbers), which hosts the guide elements. Additional masks (here blue) are needed to block the opening outside the neutron beam path. The area directly illuminated from the source is shaded yellow, the indirectly illuminated area is pale yellow. The neutron guides are not shown.

calculations Based on the model given in figure 3.10 MCNPX calculations are being performed right now. Due to the long computing time there are no results available, yet.

3.5 sample stage

The position of the stage on the floor might vary with the alignment and the operation mode of the instrument. I.e. a *x*-*y* translation stage (or a platform on air-pads)forms the basis. On top of this the co-axial horizontal rotations for 2θ and for ω are mounted, followed by an other *x*-*y* translation stage to allow for aligning the sample on the ω rotation axis. To correct tilt and roll, a *x*-*y* double goniometer is necessary. All stages above the basis could be replaced by one hexapod.

Since the sample environment can be quite heavy and voluminous, the sample stage should be able to handle wights of up to 1 t. The *free* space between the platform and the sample should be at least of the order of 300 mm.

The complete sample stage should be non-magnetic, because one principle application of this instrument will be the measurements in high magnetic fields.

motion	range	accuracy
z translation	± 20 mm	< 0.1 mm
tilt	$\pm 5^\circ$	$< 0.01^\circ$
roll	$\pm 5^\circ$	$< 0.01^\circ$
x translation	± 20 mm	< 0.01 mm
y translation	± 20 mm	< 0.01 mm
ω	$0^\circ \ldots 360^\circ$	$< 0.002^\circ$
2θ	$-5^\circ \ldots 140^\circ$	$< 0.01^\circ$
x translation	± 500 mm	< 0.1 mm
y translation	± 500 mm	< 0.1 mm

Table 3.5: Parameters for the sample stage, assuming the classical set-up using rotation and translation stages.

3.6 detector

For the reflectometry measurements one position sensitive detector is needed. The technology available today (2 mm resolution, area $400 \times 400\,\text{mm}^2$) would work. But higher resolution and a larger area would improve the instruments performance. In principle the instrument could be upgraded with a *better* detector once it is available without affecting the rest of the instrument.

According to Richard Hall-Wilton, ESS, it is realistic to expect the following parameters:

resolution:	$0.5 \times 0.5\,\text{mm}^2$	minimum
size:	$500 \times 500\,\text{mm}^2$	maximum

As consequence the highest resolution at $q = 0.01\,\text{Å}^{-1}$ with a sample-detector distance of 6.2 m, limited by the detector is

$$\begin{aligned} \Delta\theta &= \arctan[0.5/6200] \\ &\approx 0.005^\circ \\ \theta &= 0.43^\circ \quad \text{for } \lambda_{max} = 9.4\,\text{Å} \\ \Delta\theta/\theta &= 1.1\% \end{aligned}$$

The width of 500 mm results in a solid angle of $4.6^\circ \times 4.6^\circ$. This is three times the maximum divergence of the beam incident on the sample. The excess area is needed for off-specular measurements: When using λ-θ encoding, the specular beam scans over the inner 1.5°, so that effectively only another $\pm 1.5^\circ$ are available.

Since the length of the flight path is optimised to avoid the proton pulse time it is not advisable to change the sample-detector distance. So it could be mounted on a 2θ arm of fixed length, with a evacuated, frustum-shaped nozzle pointing towards the sample.

single detector For diffraction measurements on the films or the substrates a second (single) detector on a shorter 2θ arm might be used. This possibility proved to be useful e.g. to check possible bending or twinning upon cooling.

3.7 polarisation & analysis

Neutron spin polarisation and its analysis are key-features of the reflectometer for small samples. Based on the demands nowadays one can estimate at least 50% of the measurements will need a polarised beam, and at least 10% also polarisation analysis.

The concepts presented below are either well established, or under development so that there is no unknown risk connected. The choice will depend on the balancing the advantages/disadvantages. Besides to permanent coating, the options can be altered later on.

3.7.1 permanent polarisation

A permanent polarisation can be achieved using an appropriate coating on (one side of) one guide. This has the advantages that off-specular scattering from the coating will not hit the sample, and that the distance from a high magnetic field at the sample position is sufficiently large to prevent depolarisation.

3.7.2 optional polarisation

In case the 50% loss due to polarisation is not accepted, there are several approaches possible:

polarising (double bounce) reflector The ML monochromator used for λ-θ encoding or any reflector close to the initial focal point can have a polarising coating.

polarising filter By using a transmission filter with the shape of a logarithmic spiral as discussed in section B.4 it is possible to polarise a divergent beam emerging form a small source with a moderate m of the SM coating (and thus a high polarisation efficiency).

E.g. a combined λ low-pass and polariser for $\lambda \in [5, 10]$ Å, $\Delta\theta = 1.5°$, and a distance of the polariser from the focal point of 100 mm leads to a device of 350 mm length. The polarising coating has $m = 2$.

^{3}He polariser The small beam size close to the initial (intermediate) focal point allows for the operation of a rather small ^{3}He cell. Typically with a cross section of a few cm^2, only. In addition, the long distance from this point to the sample avoids depolarisation due to high magnetic fields, there.

3.7.3 analyser

The different beam geometry behind the sample demands for more complex and larger devices.

analysing filter This is the analogue to the polarising filter, but it is not realistic to install it some 100 mm behind the sample. Thus a larger multi-channel device directly in front of the detector has to be build. This is a new concept and has not been tested, yet.

wide-angle analyser based on supermirrors A SM-based multi-channel bender can be installed directly in front of the detector. Similar devices are in operation at FOCUS@PSI and at HYSPEC@SNS.

^{3}He analyser The wide divergence and the needed distance from the sample (to avoid the influence of the sample magnetic field) mean that a large ^{3}He is needed.

3.7.4 flipper

RF flipper The divergent polychromatic beam can be flipped by using a RF flipper.

switchable remanent coating For the devices based on SM coatings for polarisation / analysis one can use magnetically remanent coatings, allowing for flipping the polariser, rather than the beam.[9]

3.8 costs

The costs given below for some selected components of the instrument are based on requests to the manufacturer, on price lists and on feedback by the ESS. They display the situation beginning 2013.

insert in the extraction unit

guide SwissNeutronics made an offer for the *Selene* neutron guide and the support system on January 2013. This offer fits the parameters for the double-*Selene* guide system as discussed in section 3.4. The guide for the single-*Selene* guide system (→ 3.3 will cost about twice, proportional to the coated area.

The offer covers the neutron guide on glass or aluminium, the alignment frames, granite beams as a base and an aluminium housing to contain the vacuum. This does not exactly match the requirements by the ESS, since shielding issues most likely will not allow for the offered wide and straight vacuum housing and the alignment system with frames. But it still gives an idea of the actual costs to be expected. For the guides the offer covers the curved substrates with a $m = 2.5$ Ni/Ti coating. In detail there are 4 guide sections of 7.2 m, each, consisting of 15 elements, made up of 2 truly curved mirrors.

double-*Selene* guide system 550 k€

guide support The support consists of 4 granite beams on kinematic mounts, the alignment frames, the vacuum housing, and vacuum windows. No shielding is included. Mounting is due to the customer.

guide support 520 k€

sample stage (HUBER, JJ-XRAY)

detector (ESS)

filter / polariser (Uwe)

3.9 discussion

C data reduction

C.1 raw-data and intensity maps

Each neutron detected on the position sensitive detector has the associated parameters t, y and z for the time-of-flight and the position on the detector. The detector spatial resolution gives the constant values Δy and Δz, the pulse length sets an upper limit for $\Delta t <= \tau$. The latter one might be reduced by choppers.

From theses basic parameters and the instrument parameters X (source detector distance) and θ_{detector} one can calculate the neutron wavelength [→**??**]

$$\lambda = \frac{h}{m_n}\frac{t}{X} \tag{C.1.1}$$

and the final angle after reflection

$$\theta_f = \hat{\theta} + \omega - \arctan z \tag{C.1.2}$$

where ω is the inclination of the sample surface relative to the long axis of the last ellipse of the *Selene* guide, z is the position on the detector if that one is located at $\theta_{\text{detector}} = \hat{\theta} + 2\omega$.

Discretisation in λ and θ_f of a large ensemble of events gives the intensity map $I(\lambda, \theta_f)$ with the error-map $E(\lambda, \theta_f) \approx \sqrt{I(\lambda, \theta_f)}$. The approximation is valid for more than 10 counts per bin. For less counts a correcting factor has to be taken into account. Zero counts is also a measured quantity and has to have an error. This topic has to be investigated further!

It is also possible to extract $I(q_z)$, $E(q_z)$ or $I(q_z, q_x)$, $E(q_z, q_x)$, instead. ...

C.2 normalisation

The measured intensity map $I(\lambda, \theta)$ is not only a function of $R(q_z)$ of the sample, but also of the intensity $I_{\text{sample in}}(\lambda, \theta, x, y)$. incident on it. This quantity could ideally be measured with a reference sample with $R(q) = 1$ and exactly the same shape and position as the sample. Non-perfect reflectivity can be corrected for as long as $R_{\text{reference}}(q)$ is known and homogeneous. One could e.g. use a supermirror-coated reference with $m = 10$ (and low reflectivity) to correct up to $q_z = 0.22\,\text{Å}^{-1}$.

For higher q_z this approach is unrealistic. On the other side the projected sample height is larger, which leads to an averaging over beam inhomogeneities. So it might be possible to use a calculated or simulated reference. The quality of the calculation or simulation can be checked by comparison to the reference below $q_z = 0.22\,\text{Å}^{-1}$.

integration normal to the scattering plane The normalisation can be performed after integrating in y direction on the detector, i.e. normal to the scattering plane. This is justified by

$$\begin{aligned} I(t, y, z) &= I(t, z) \cdot g(y) \\ \frac{\int I(t, y, z)\,\mathrm{d}y}{\int I_0(t, y, z)\,\mathrm{d}y} &= \frac{\int I(t, z)\, g(y)\,\mathrm{d}y}{\int I_0(t, z)\, g(y)\,\mathrm{d}y} \\ &= \frac{I(t, z)\ \int g(y)\,\mathrm{d}y}{I_0(t, z)\ \int g(y)\,\mathrm{d}y} \\ &= R(t, z) \end{aligned}$$

where $g(y)$ gives the intensity distribution in y direction. By using a single detector or a 1D position sensitive detector this integration is already realised. This is the case in many conventional reflectometers.

C.3 resolution

In most cases the resolution function $f(q_z)$ with $R_e(q_z) = R(q_z) * f(q_z)$ will neither be constant nor proportional to q_z. It is thus dangerous to add several data sets, e.g. obtained with various ω.

C.3.1 summation of data sets with different resolution

The summation of data sets $R_i(q_z)$ with different resolution $f_i(q_z)$ is possible, but it leads to a complicated (i.e. not single-Gaussian) resolution function:

$$
\begin{aligned}
R_\Sigma &= \sum_i a_i R_i \quad , \quad \sum_i a_i = 1 \\
&= \sum_i a_i R * f_i \\
\mathcal{F}[R_\Sigma] &= \mathcal{F}\left[\sum_i a_i R * f_i\right] \\
&= \sum_i a_i \mathcal{F}[R * f_i] \\
&= \sum_i a_i \mathcal{F}[R] \cdot \mathcal{F}[f_i] \\
&= \mathcal{F}[R] \cdot \sum_i (a_i \mathcal{F}[f_i]) \\
&= \mathcal{F}[R] \cdot \mathcal{F}\left[\sum_i a_i f_i\right] \\
&= \mathcal{F}\left[R * \left(\sum_i a_i f_i\right)\right] \\
R_\Sigma &= R * \left(\sum_i a_i f_i\right) \\
&:= R * f_\Sigma
\end{aligned}
$$

Simulation or fitting of $R(q_z)$ is possible when $f_\Sigma(q_z)$ can be estimated, and when is taken into account in the simulation software.

For publication such a reflectivity profile might not be suited because the abrupt changes in $f_\Sigma(q_z)$ at the joints can lead to peaks or dips in R_Σ.

C.3.2 convolution to $\Delta q/q = \text{const}$

In cases when the experimental resolution function $f_e(q)$ of one data set $R_e(q) = R(q) * f_e(q)$ is known, one can convolve $R_e(q)$ with a resolution $f_c(q)$ in a way to get $R_p(q)$ with $\sigma_p \propto q$, i.e. $\Delta q/q = \text{const} := p$. For Gaussian the relation

$$
\begin{aligned}
f_{e/c}(q) &= \frac{1}{\sqrt{2\pi}\,\sigma_{f/c}} \exp\left[-\frac{(q - q_{f/c})^2}{2\sigma_{f/c}^2}\right] \\
f_p(q) &= f_e(q) * g_c(q) \\
&= \frac{1}{\sqrt{2\pi}\,\sigma_p} \exp\left[-\frac{(q - q_p)^2}{2\sigma_p^2}\right] \qquad \text{with} \quad \sigma_p^2 = \sigma_e^2 + \sigma_c^2, \quad q_p = q_e + q_c
\end{aligned}
\tag{C.3.1}
$$

holds. For the present case $q_{e/c} = 0$. So when $\sigma^e(q)$ is known one can get the *correcting Gaussian* with

$$
\sigma_c(q) = \sqrt{p^2 q^2 - \sigma_e^2(q)} \tag{C.3.2}
$$

with $\sigma_p = p\,q$. Avoiding $\sigma_c <= 0$ leads to the constraint

$$
p > \frac{\sigma_e(q)}{q} \quad \forall q
$$

The resulting *corrected* reflectivity curve is then

$$\begin{aligned} R_p(q) &= R_e(q) * f_c(q) \\ &= \int_{\bar{q}=q_{\min}}^{q_{\max}} R_e(q-\bar{q}) \cdot \frac{1}{\sqrt{2\pi}\,\sigma_c(\bar{q})} \exp\left[-\frac{\bar{q}^2}{2\sigma_c(\bar{q})^2}\right] \mathrm{d}\bar{q} \end{aligned} \tag{C.3.3}$$

This now allows to merge several data sets after bringing them the the same resolution for each q in the overlapping region. Of cause information is lost by lowering the resolution, but the resulting $R_e(q)$ and eventually a merged $R_\sigma(q)$ have the appearance expected by standard software, most of the users, and almost all readers of publications.

!!! Besides the resolution of the data imposed by the experiment and the data analysis, there is the resolution of the representation of the data, I.e. the spacing of the nodes. To be able to distinguish peaks in $R(q_z)$, already convoluted with the final resolution function $f(q)$, one has to .....

From δq (FWHM) to σ:

$$\exp\left[\frac{q_{1/2}^2}{2\sigma^2}\right] = 0.5 \tag{C.3.4}$$

$$q_{1/2} = \sqrt{2\ln 2}\sigma \tag{C.3.5}$$

$$\Delta q = 2\,q_{1/2} \tag{C.3.6}$$

$$\approx 2.3548\,\sigma \tag{C.3.7}$$